photonics

MDPI

Article

Optical Coherence Tomography for In-Situ Alignment Inspection of Hairpin Ends in EV Stator Laser Welding

Yingjian Wang [1], Bixia Wang [1], Lang Xu [1], Xiaolin Liu [1], Qi Chen [2], Xiaodong He [2], Jianwu Wu [2] and Yaoyu Ding [1,*]

[1] School of Automation Engineering, University of Electronic Science and Technology of China, Chengdu 611731, China; 202421060122@std.uestc.edu.cn (Y.W.); 202422060137@std.uestc.edu.cn (B.W.); 202421060136@std.uestc.edu.cn (L.X.); 202521060120@std.uestc.edu.cn (X.L.)

[2] Wenzhou Institute of Industry & Science, Whenzhou 325000, China; cq@wzgky.com (Q.C.); hxd@wzgky.com (X.H.); wjw@wzgky.com (J.W.)

* Correspondence: yding@uestc.edu.cn; Tel.: +86-18180688899

Abstract

Laser welding of hairpin ends is a key joining process for electric-vehicle (EV) traction motors, but pre-weld geometric deviations—including lateral gap variation, axial height mismatch, and focus offset—can compromise weld stability and long-term motor reliability. Conventional coaxial camera inspection provides reliable two-dimensional information but cannot directly measure axial mismatch or local end-face topography. To address this limitation, this study applies a coaxial in-line inspection system that integrates a spectral-domain optical coherence tomography (OCT) depth-sensing path and a CMOS visual imaging channel into a common optical axis. Unlike conventional OCT applications that aim for multilayer subsurface imaging in transparent media, the OCT channel in this work profiles the single reflective interface of opaque copper end faces and achieves axial linear residual errors within ±15 μm over a 4.5 mm working range, given an approximately 900 mm focus distance. The visual channel locates the weld seam and evaluates in-plane longitudinal stagger, whereas the OCT channel performs fixed-position B-scan profiling for lateral gap, axial height mismatch, end-face topography defects, and focus-offset assessment without requiring vision-guided scan repositioning. Experiments on 16 hairpin-end mock-up pairs, including 13 intentionally introduced defect samples, achieved correct classification for all tested samples. The OCT depth-profiling step was completed within the visual inspection time window, enabling parallel OCT–visual inspection without extending the original production takt time. These results demonstrate the feasibility of this non-contact method for pre-weld quality assurance in the EV stator laser welding scenario.

Keywords: optical coherence tomography; laser welding; hairpin winding; EV stator; in situ alignment inspection

Check for updates

Received: 24 July 2026
Revised: 19 October 2026
Accepted: 22 October 2026
Published: 27 October 2026

Copyright: © 2026 by the authors. Licensee MDPI, Basel, Switzerland. This article is an open access article distributed under the terms and conditions of the Creative Commons Attribution (CC BY) license.

1. Introduction

The rapid growth of the electric vehicle (EV) industry requires motor manufacturing processes with high throughput, high repeatability, and low defect rates [1,2]. Hairpin winding has become a mainstream architecture for EV traction motors because it provides a high slot fill factor, improved thermal performance, and strong compatibility with automated assembly [3,4]. In this architecture, the stator winding is formed not from round wire but from preformed rectangular copper conductors, called hairpins because of their U-shape before assembly. The hairpins are inserted into the stator slots, their open ends are bent to a prescribed angle, and the ends of adjacent conductors are then joined to form the

continuous winding circuit [5,6]. The rectangular cross-section fills the slot more completely and conducts heat more effectively to the stator core than round wire, which supports the high power density and efficiency required of EV traction motors. A single stator contains a large number of weld joints, each of which carries the winding current; the quality of every individual joint therefore directly affects the electrical resistance, heating, and long-term reliability of the motor. Laser welding is widely used for this joining step because it offers high processing speed and localized energy input [7,8]. Nevertheless, weld quality is sensitive to the relative position and end-face condition of the paired copper conductors. Excessive lateral gap, longitudinal stagger, axial height mismatch, or irregular end-face morphology can cause unstable coupling of laser energy, incomplete fusion, porosity, or weak joints, which may increase electrical resistance and reduce motor reliability [9–11].

In current hairpin-stator production lines, pre-weld quality control is typically implemented through automated positioning, camera-based seam localization, and dimensional checks [12]. These methods are compatible with high-throughput manufacturing and can efficiently identify macroscopic placement errors, weld-surface anomalies, or electrical discontinuities [13]. However, laser welding of rectangular copper hairpins is strongly affected by the relative height of the two end faces, the lateral gap, local end-face topography, and the focus condition at the actual welding coordinate. Conventional two-dimensional vision provides robust in-plane information but cannot directly measure axial height mismatch or cross-sectional surface profiles with the required depth precision. Laser triangulation and structured-light methods can provide additional geometric information and, on diffuse or moderately reflective surfaces, have been reported to achieve accuracies on the order of 0.01–0.1 mm [14,15]; however, on highly specular, opaque copper end faces such as those addressed in this work, both approaches are prone to signal saturation, multi-path reflection, and localized point-cloud dropout, typically requiring dedicated image-processing strategies (e.g., multi-peak evaluation or hole-filling) to remain usable [16,17]. In addition, these techniques generally require an offset viewing or projection angle relative to the surface normal, which complicates their integration into a coaxial optical path shared with the welding beam and their registration to the laser processing coordinate.

Optical coherence tomography (OCT) is an established non-contact, depth-resolved imaging technique that acquires depth-resolved A-scans through low-coherence interferometry and constructs B-scan cross-sectional images from sequential A-scans; it has been applied to industrial surface metrology, layer-thickness measurement, and laser process monitoring [18–25]. Physically, OCT shares the same low-coherence interferometric principle as coherence scanning interferometry (also known as white-light interferometry), an established surface-metrology technique that similarly derives depth information from the localization of low-coherence interference fringes, differing mainly in the axial depth-encoding strategy and in application-community conventions [26,27].

A further consideration, distinct from this shared interferometric principle, concerns the working distance achievable by an OCT system's sample-arm optics, which is sometimes conflated with the axial imaging depth range but reflects a separate design trade-off. The axial imaging depth range is determined primarily by the source coherence properties and detection scheme, and is not, in principle, fundamentally limited: using a long-coherence-length swept source together with specialized photonic receiver hardware and signal processing, 3D OCT imaging has been demonstrated over a 1.5 m depth range at 15 µm axial resolution and a 100 kHz A-scan rate [28]. The working distance of the sample-arm focusing optics, in contrast, is governed by the trade-off between numerical aperture, focused spot size, and lens aperture: for a fixed spot size, extending the working distance requires a proportionally larger aperture to maintain the same numerical aperture, which becomes impractical for very long standoff distances unless the required spot size is correspondingly

relaxed. The approximately 900 mm working distance of the coaxial system developed in this work, together with its approximately 50 μm ($1/e^2$) focused spot at 837.2 nm, corresponds to a numerical aperture of approximately 0.011, implying a focusing-lens aperture on the order of 20 mm—modest enough to be practical rather than requiring an impractically large lens. This working distance is dictated by the standoff requirement of the coaxial laser welding head, and is practical here specifically because the pre-weld alignment task tolerates a comparatively large spot size and depth of focus, in contrast to the much tighter lateral resolution requirements of typical biomedical or high-resolution industrial OCT probes, for which a working distance of this scale would not be practical regardless of the achievable depth range.

In the context of laser welding specifically, OCT has been increasingly adopted as a versatile inline monitoring technology spanning the pre-, in-, and post-process stages [29]. Most reported applications, however, address in-process monitoring, such as keyhole depth and melt-pool fluctuation measurement during copper laser welding [30], weld-penetration-depth monitoring via coaxially aligned dual measurement beams for automotive battery tab connectors [31], and coaxial seam-tracking for the detection of beam-to-workpiece misalignment during welding of hidden joints [32], as well as recent multi-sensor gap-prediction approaches for copper overlap joints combining OCT with imaging and spectroscopic sensors [33]; a recent review provides a comprehensive survey of this rapidly growing body of work [34]. Specifically for hairpin-winding motors, a preliminary study has outlined the potential of OCT for pre-, in-, and post-process monitoring of hairpin laser welding based on first exploratory experiments, noting the absence of prior scientific studies on this application at the time [35].

Relative to this prior work, three gaps remain unaddressed. First, the in-process monitoring studies measure keyhole depth, melt-pool behavior, or weld-penetration depth during welding, and do not address the pre-weld geometric qualification (gap, stagger, height mismatch, end-face topography, focus offset) needed before the weld is made. Second, the prior work specific to hairpin winding welding reports first exploratory experiments intended to outline OCT's potential for this application, without a system-level characterization (PSF, SNR, axial repeatability, defocus response) or a multi-defect experimental validation across a defined taxonomy of pre-weld defect types. Third, none of the cited studies combine OCT with a parallel visual channel operating at a fixed, welding-registered coordinate, a configuration whose processing latency this work explicitly quantifies to demonstrate compatibility with production takt time.

The present work addresses all three gaps. It applies OCT surface profiling to the pre-weld inspection of opaque copper hairpin ends, and, by combining OCT depth measurement with visual seam recognition in a parallel visual–OCT strategy, synchronously evaluates in-plane stagger, lateral gap, axial height mismatch, end-face topography, and defocus directly at the welding station, avoiding the latency associated with sequential vision-guided depth scanning.

Accordingly, this paper presents a hybrid coaxial inspection system for pre-weld hairpin-end assessment. The system combines image-based visual recognition and spectral-domain OCT through a shared optical path with the high-power laser welding beam. The OCT B-scan region is assigned according to the fixed workpiece coordinate used for welding, so the depth measurement does not depend on prior visual guidance. The two channels are complementary. A single OCT B-scan acquired perpendicular to the seam resolves the cross-sectional profile of the two end faces, and hence the lateral gap, axial height mismatch, end-face topography, and focus offset, but it carries no information along the seam direction, so a longitudinal (Y-axis) stagger between the two hairpins cannot be obtained from it. The camera supplies this missing in-plane information by imaging the full

end-face region, locating the seam, and measuring the Y-stagger from the detected end-face contours. Combining the two channels therefore provides all five geometric indicators within a single inspection step. In addition, camera-based seam localization is already part of existing production-line inspection, so the OCT depth profiling is added to an existing visual step and runs in parallel with it. The proposed workflow is intended for rapid pre-weld screening at the welding station rather than for volumetric subsurface inspection.

2. System

2.1. Coaxial Optical System Architecture

The schematic of the coaxial detection system is shown in Figure 1a, and the corresponding CAD model of the coaxial optical layout is shown in Figure 1b. The optical layout combines three channels—namely, the welding laser, the OCT probe beam, and the visible imaging path—along a common axis so that the measured region is registered to the subsequent welding position.

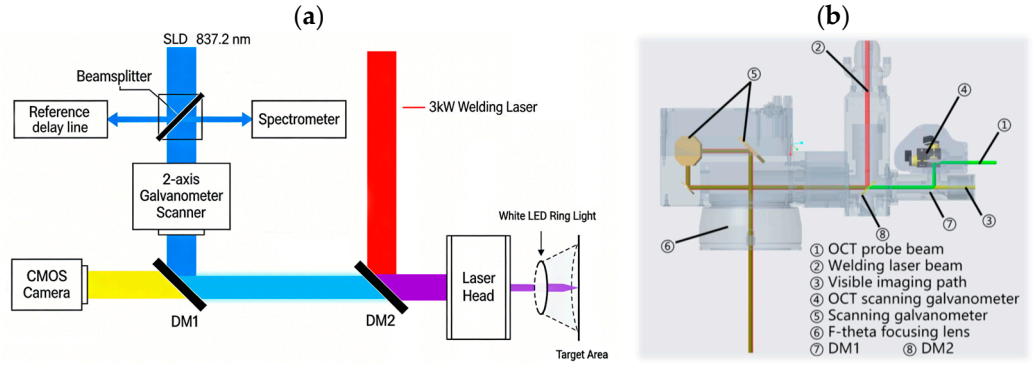


Figure 1. (**a**) Schematic diagram of the coaxial optical detection system integrating the laser welding beam, OCT probe beam, and visual imaging channel; (**b**) CAD model depicting the coaxial optical layout.

The OCT channel is configured as a spectral-domain OCT interferometer. A fiber-pigtailed superluminescent diode (SLD-37-HP, Superlum, Cork, Ireland) provides broadband illumination with a measured center wavelength of 837.2 nm, a full-width at half-maximum bandwidth of 53.5 nm, and an output power of approximately 25 mW. A 50/50 fused fiber coupler (FUSED-22-850-5/125-50/50, OZ Optics, Ottawa, ON, Canada) divides the source light into reference and sample arms. In the reference arm, a collimated beam is reflected by a retroreflector mounted on a motorized translation stage for optical path-length adjustment. In the sample arm, the collimated OCT beam is delivered to the laser processing head and combined coaxially with the visible imaging path and the 1064 nm welding laser.

The OCT sample beam is steered by a two-axis galvanometer scanner (Compact 506, ScannerMAX, Hudson, MA, USA) to acquire B-scans across the weld seam. Coaxial beam combination is implemented with two dichroic mirrors (DM1: 69–207, DM2: 96–688, Edmund Optics, Barrington, NJ, USA) selected according to the spectral bands of the visible camera, the OCT probe, and the welding laser. DM1 transmits the visible band and reflects the OCT wavelength, whereas DM2 transmits the visible and OCT bands and reflects the 1064 nm laser. The optical arrangement in Figure 2 allows the three channels to share a common inspection and processing axis while limiting inter-channel spectral crosstalk.

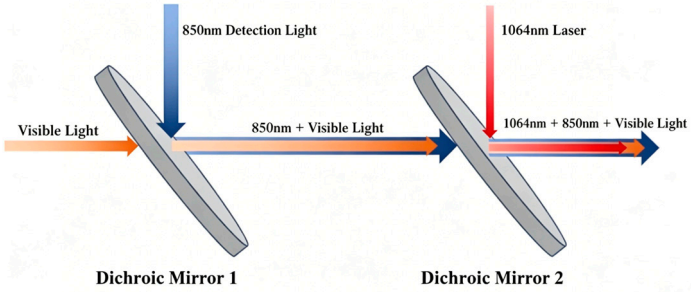


Figure 2. Schematic diagram of the dichroic mirror arrangement for coaxial combination of the visible imaging, OCT, and laser welding beams.

Specifically, DM1 provides high transmission in the 400–725 nm visible band and high reflection near 850 nm for the OCT probe, while DM2 transmits the visible and OCT wavelengths and reflects the 1064 nm laser. This spectral separation registers the camera image, OCT B-scan, and laser processing position without mechanical switching between sensors.

The welding source is a 3 kW continuous-wave fiber laser (HWC-3000-MM, Han's Laser, Shenzhen, China) operating at 1064 nm. Its output is reflected by DM2 and combined with the OCT and visible channels downstream of the dichroic mirrors. The combined beam path then enters the laser processing head (SS-IV-30 scanning head with F-theta focusing lens, RAYLASE, Wessling, Germany), which contains a large-aperture scanning mirror and a focusing lens for delivery to the workpiece. This arrangement supports pre-weld OCT profiling and subsequent laser processing at the same nominal coordinate.

Back-scattered OCT light from the sample retraces the illumination path, re-enters the fiber coupler, and interferes with the reference beam. The resulting spectral interferogram is recorded by a custom spectrometer (CD800S-840/60-250-OC2K-CL, Wasatch Photonics, Durham, NC, USA) equipped with a 1 × 2048-pixel line-scan CMOS sensor (OctoPlus, Teledyne e2v, Chelmsford, UK) operating at an A-scan rate of 82.5 kHz. The sample-arm reference position was set such that the working range of interest remained entirely on one side of the zero-delay line, so that the mirror (complex-conjugate) image did not overlap with the region containing the hairpin end-face surface and was discarded during processing. After k-linearization, background-spectrum subtraction, and Fourier transformation, each A-scan yields 1024 usable depth pixels within the single-sided imaging depth, corresponding to an imaging depth of approximately 5.9 mm in air. The sample beam is focused to an approximately 50 μm diameter spot ($1/e^2$) on the target surface, with a depth of focus of about 5 mm. These parameters define the lateral sampling scale and the tolerance to height variation during hairpin-end inspection. The axial resolution was characterized experimentally from the point spread function (PSF) obtained with the flat silicon plate described in Section 2.2; a Gaussian fit to the measured PSF yielded a full-width-at-half-maximum (FWHM) of 35.165 ± 6.660 μm, which was adopted as the reported axial resolution of the system in preference to a theoretical value calculated from the source spectral parameters. It should be noted that this FWHM value characterizes the width of the point spread function rather than the achievable precision in localizing the peak position of a reflective surface, which is the quantity relevant to surface profiling applications. This localization precision depends on the signal-to-noise ratio and the surface-position estimation algorithm employed rather than on the nominal resolution alone [36].

Figure 3 shows the assembled system, in which a monochrome CMOS camera module (DH3069-4122-9281, based on the OV9281 CMOS sensor, OmniVision Technologies, Santa Clara, CA, USA; 1 Mpixel, global shutter), fitted with a machine-vision lens (M35F18-5MP), is coupled through the transmission channel of DM1 for visual imaging. Visible

illumination is provided by a white LED ring light mounted in front of the laser head. The ring has an outer diameter of 180 mm, an inner diameter of 120 mm, and a 60° illumination angle, providing uniform illumination over the camera field of view without blocking the coaxial path. Reflected visible light propagates back through DM2 and DM1 and is imaged by a broadband lens onto the CMOS sensor. The lens provides an approximately 43 mm × 27 mm field of view at the working distance, and the camera frame rate of up to 120 fps is sufficient for real-time seam localization.

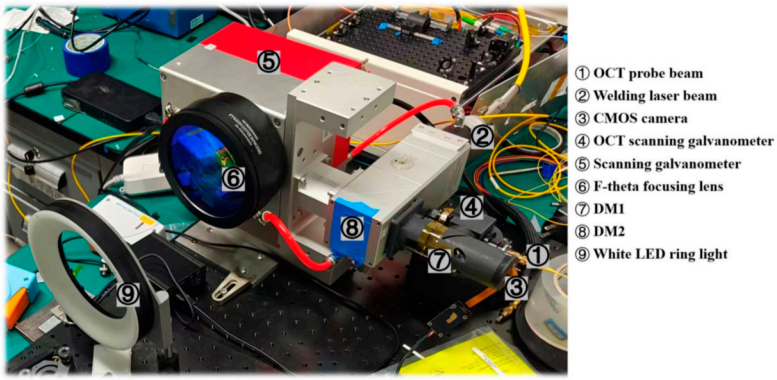


Figure 3. Photograph of the integrated OCT–laser welding system.

During operation, the system is positioned over the stator end-winding region. The visual camera and OCT scanner are triggered by the central controller and operate in parallel under ring-light illumination. The coaxial configuration reduces parallax between the sensing region and the welding region.

2.2. System Performance Characterization

The metrological performance of the integrated coaxial system was evaluated for both the OCT depth-sensing channel and the visual imaging channel. For the OCT subsystem, the point spread function (PSF), A-scan signal-to-noise ratio (SNR), axial repeatability over the working range, and defocus-dependent signal response were characterized, as shown in Figure 4. The lateral measurement performance of the visual imaging channel was evaluated using a calibrated checkerboard target.

To characterize the PSF and the A-scan SNR, a flat silicon plate was positioned near the focal plane and one typical interference spectrum was acquired. As the acquired spectrum did not uniformly fill the full spectral range of the line-scan detector, a Hann window was applied prior to Fourier transformation, with its extent and position adjusted to match the region of the detector array containing usable spectral signal, in order to suppress spectral leakage associated with the effectively truncated spectral edge. After background subtraction, k-space resampling, Hann-window apodization, and Fourier transformation, the A-scan magnitude profile was obtained, as shown in Figure 4a. The A-scan magnitude profile was first evaluated in linear intensity units. The surface reflection peak was fitted with a Gaussian function, and the maximum intensity of the fitted peak was used as the signal intensity. The noise intensity was calculated as the mean linear intensity of two flat background windows far from the peak, with 20 sampling points selected on each side. The resulting peak-to-background ratio was then converted to dB for reporting. Therefore, the SNR reported here represents a single-A-scan peak-to-background contrast rather than the sensitivity-based SNR convention commonly used in biomedical OCT. This procedure yields a peak-to-background contrast of 21.7 dB, which is adequate for extracting the reflective copper surface and the inter-hairpin gap in the intended industrial inspection task.

To evaluate axial repeatability over the working range expected for hairpin ends, the same silicon plate was translated away from focus in 0.5 mm increments over a 4.5 mm travel range using a manual precision translation stage (HX65, Hengyang Optics) with a micrometer-type adjustment mechanism, a minimum graduation of 0.01 mm, a manufacturer-specified sensitivity of 0.002–0.003 mm, and a straightness of 0.003 mm. As the specified straightness and sensitivity of the stage are approximately an order of magnitude smaller than the axial residual errors reported below, the stage was considered an adequate reference for the present characterization without additional independent calibration. At each position, a B-scan was recorded and the PSF peak depth was used as the measured displacement. The measured displacement remained highly linear with respect to the reference stage movement, with residual errors within ±15 μm over the full range, as shown in Figure 4b. This residual is of the same order as the ±10 μm short-term fluctuation characterized below and is therefore attributed primarily to the same underlying mechanical vibration, with a smaller contribution from manual positioning variability of the translation stage during the step-by-step adjustment. Short-term stability was examined by collecting 2000 consecutive A-scans at each stepped position while the plate was stationary. As summarized in Figure 4c, the measured peak depth fluctuated by less than ±10 μm at all tested positions, confirming the axial repeatability of the coaxial OCT channel. The residual short-term fluctuation is attributed primarily to mechanical vibration transmitted through the optical mounts and the shared platform supporting the laser processing head, as the setup was not mounted on a vibration-isolated optical table; this is consistent with the intended industrial deployment environment, and the reported fluctuation therefore reflects performance under representative, rather than laboratory-optimized, mechanical conditions.

The dependence of OCT signal intensity on defocus was characterized using the flat silicon plate. The plate was initially positioned at the focal plane and then translated away from focus in 0.5 mm increments over a total travel range of 4.5 mm. At each position, the A-scan peak intensity was recorded. As shown in Figure 4d, the signal reaches its maximum near the nominal focal plane and decreases monotonically with increasing defocus. Using a 2 dB reduction from the peak intensity as the criterion, the measured one-sided depth of focus is approximately 3 mm. With a 3 dB criterion, the effective one-sided detection range extends to approximately 4 mm, which covers the expected height variation of the tested hairpin-end samples.

The lateral measurement accuracy of the visual channel was assessed separately with a precision checkerboard target placed at the working distance. The target, which carried square grids of precisely known dimensions, was imaged under ring-light illumination. Grid corner coordinates were extracted, and the distances estimated from the image within the central 6 mm × 6 mm region were compared with the known reference values, with deviations in both axes consistently within ±30 μm. This lateral deviation is attributed primarily to residual geometric distortion of the replacement machine-vision lens (M35F18-5MP, 35 mm focal length, f/1.8, 2/3-inch image format), which was substituted for the default lens supplied with the CMOS camera module (OV9281) to achieve a field of view compatible with the hairpin end-face inspection area; no dedicated lens-distortion calibration was performed. As geometric distortion is generally most pronounced toward the periphery of the field of view, its effect on the reported lateral accuracy is expected to be reduced by restricting the accuracy evaluation to the central 6 mm × 6 mm region, though residual distortion, together with sub-pixel localization uncertainty in the checkerboard corner-detection algorithm and minor non-uniformity in the ring-light illumination, likely contributes to the observed deviation.

Together, these results show that the coaxial architecture provides the axial repeatability, signal robustness, defocus tolerance, and lateral measurement precision required for rapid pre-weld inspection of hairpin stators.

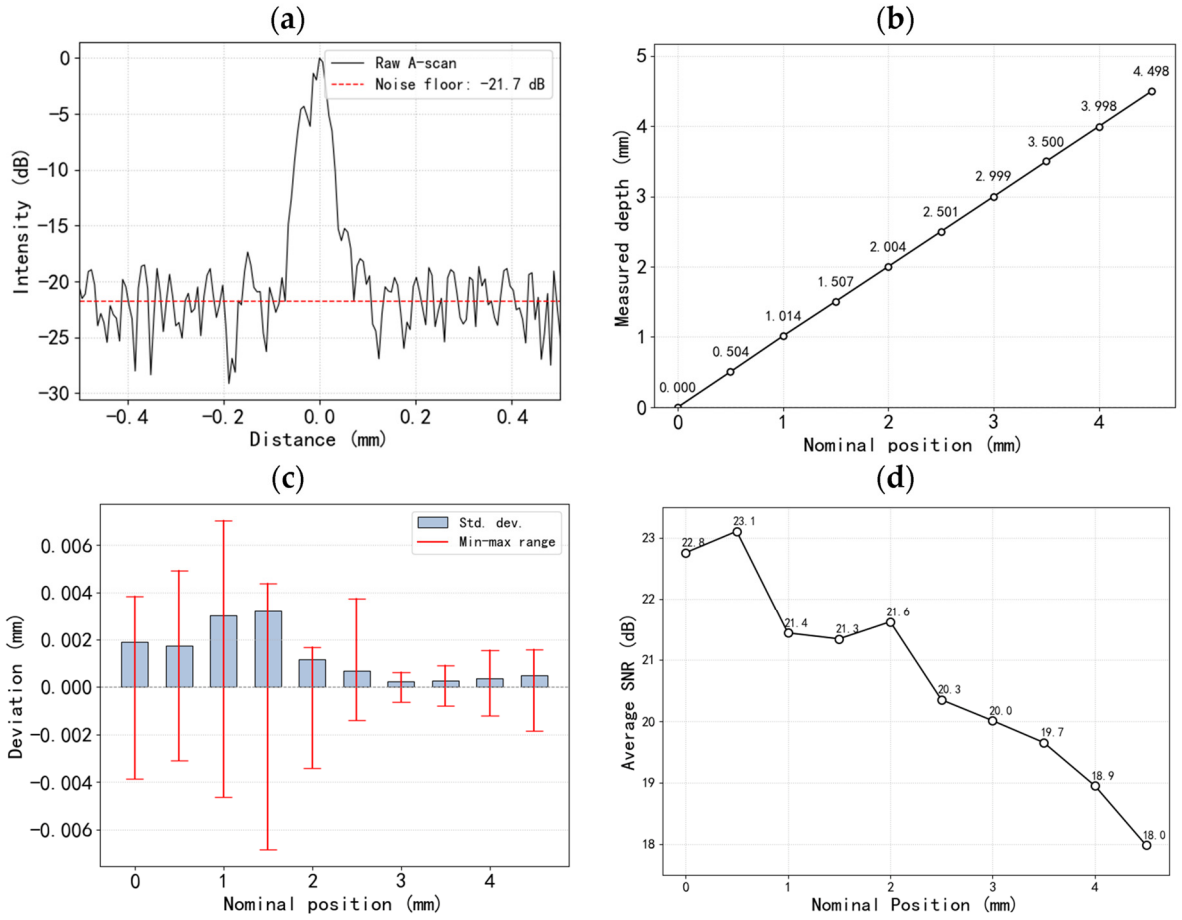


Figure 4. OCT and visual-channel performance characterization. (**a**) Depth point spread function (A-scan), where the fitted surface peak is used as the signal and two flat background windows of 20 points each are used to estimate the noise, yielding a single-A-scan SNR of 21.7 dB. (**b**) OCT axial displacement measurement linearity across a 4.5 mm working range, showing residual displacement errors within ±15 µm relative to the reference stage movement. (**c**) OCT depth measurement repeatability over a 4.5 mm working range, with measured peak-depth fluctuations within ±10 µm. (**d**) OCT sensitivity versus defocus: peak intensity as a function of distance from the focal plane; a 2 dB drop defines a one-sided depth of focus of approximately 3 mm, and a 3 dB drop extends the effective detection range to approximately 4 mm.

2.3. Integrated Visual-OCT Parallel Inspection for Weld Seam Defect Detection

The inspection workflow combines the Y-stagger obtained from the visual channel with the depth-domain indicators obtained from the OCT channel to generate a unified welding decision. As summarized in Figure 5, both channels are triggered synchronously by the central controller. The OCT branch performs fixed-position B-scan profiling at the welding coordinate, while the visual branch provides the seam position and longitudinal-stagger information. If any parameter exceeds its corresponding process threshold, including excessive lateral gap, height mismatch, end-face topography anomaly, defocus, or longitudinal stagger, the controller rejects the weld position and reports the defect category.

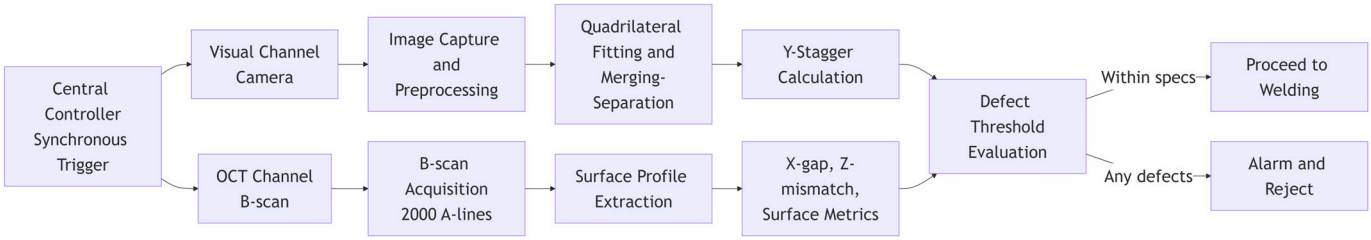


Figure 5. Parallel processing workflow of the coaxial visual–OCT inspection system.

For the OCT branch, a single B-scan is acquired perpendicular to the weld centerline at the preset welding coordinate. The scan contains 2000 A-scans over an approximately 5 mm lateral range, forming a cross-sectional surface profile of the two copper end faces and the inter-hairpin gap. Because the copper end faces are opaque and highly reflective, the measurement is treated as single-interface surface profiling rather than multilayer tomographic reconstruction.

Surface extraction from the B-scan is performed by intensity segmentation of the copper reflections, morphological closing of small discontinuities, and connected-component analysis of the left and right hairpin surfaces.

For each lateral column, the mean row coordinate of the segmented surface pixels is recorded to form a one-dimensional end-face profile, as shown in Figure 6a. Based on this OCT-derived profile, the X-gap is calculated from the boundary separation between the two connected components, the Z-height mismatch is calculated from the difference between their mean surface depths, and surface abnormality is quantified by the height range of each component.

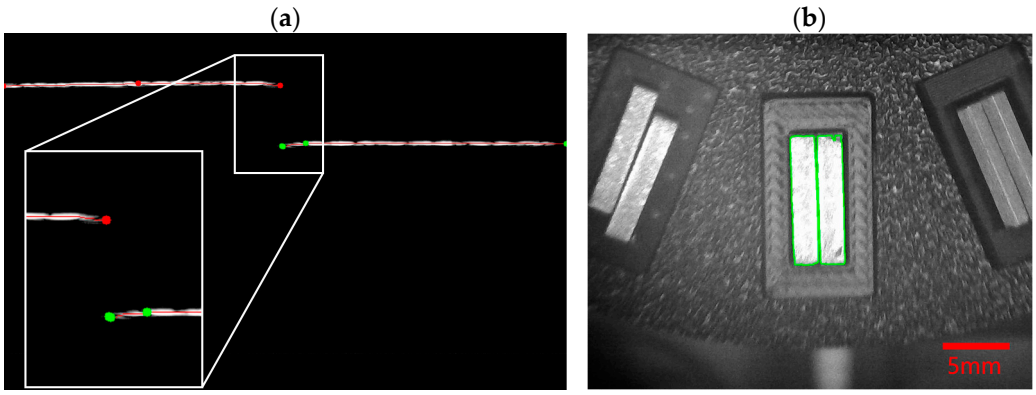


Figure 6. Typical OCT and visual inspection results. (**a**) Processed B-scan with extracted surface points overlaid in red; (**b**) Camera image of the hairpin end faces with the detected end-face contours overlaid in green.

The visual branch supplies the in-plane information that is not available from this fixed OCT B-scan. After thresholding and contour extraction of the hairpin end-face image, the two hairpin end-face regions are approximated by quadrilaterals, as shown in Figure 6b, and the seam centerline and short-edge correspondence are used to estimate the Y-stagger.

The OCT-derived indicators are compared with the predefined process tolerances immediately after acquisition. To quantify the total latency of the inspection pipeline, the processing time of each stage was measured on a workstation equipped with an AMD Ryzen 7 4800H processor (2.90 GHz), 16 GB RAM, and an NVIDIA GeForce RTX 2060 GPU (6 GB). A single OCT B-scan is acquired in 0.024 s and subsequently processed—including surface segmentation, morphological closing, and connected-component-based extraction of the X-gap, Z-height mismatch, and surface height range—within 0.088 ± 0.004 s. In

parallel, the visual branch requires 0.059 ± 0.008 s for image processing, including contour extraction and Y-stagger estimation. Because the OCT and visual branches are triggered simultaneously and executed concurrently on separate processing threads, the total pipeline latency is determined by the longer of the two branches rather than their sum. The resulting total pipeline latency is therefore approximately 0.112 s, which remains within the existing visual-inspection time window of the production station, confirming that the added OCT depth-sensing capability does not extend the original production takt time.

3. Experimental Setup

3.1. Ideal End-Face Alignment and Defect Taxonomy

In an ideal laser welding scenario for hairpin stators, the two copper hairpin ends in a weld pair should have coplanar end faces, a controlled lateral gap, and no longitudinal stagger along the seam direction, while the laser focal plane should be accurately aligned with the common end-face plane. In the experiments, rectangular copper coupons of 10 mm (Y axis) × 2 mm (X axis) × 50 mm (Z axis) were used to represent individual hairpin ends, and two coupons placed side by side formed the weld-seam analogue.

Three relative-position defects and two end-face topography defects were considered: excessive *X*-axis gap, *Y*-axis stagger, *Z*-axis height mismatch, sawtooth (V-groove) topography, and single-sided inclined end-face defect. Together with the nominal reference pair, these cases cover the main pre-weld geometric conditions relevant to laser joining of hairpin ends, as shown in Figure 7.

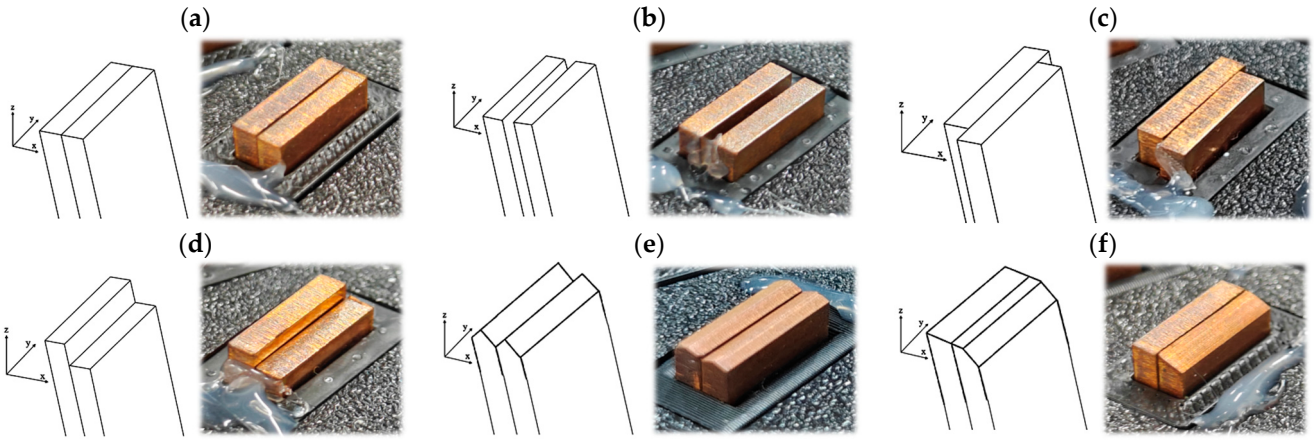


Figure 7. Schematic diagrams (**left**) and photographs (**right**) of the ideal hairpin end-face pair and the five defect types. (**a**) Defect-free nominal pair. (**b**) *X*-axis gap defect. (**c**) *Y*-axis stagger defect. (**d**) *Z*-axis height mismatch defect. (**e**) Sawtooth (V-groove) defect. (**f**) Single-sided inclined end-face defect.

3.2. Fabrication of Defect Samples

Relative-position defects were introduced using customized 3D-printed holders with different seating geometries. The *X*-axis gap was controlled by inserting a central partition between the two coupons, the *Y*-axis stagger was produced by offsetting the seating positions along the seam direction, and the *Z*-axis height mismatch was generated by using stepped support surfaces with different heights.

Four X-gap levels (0.25, 0.50, 0.75, and 1.00 mm), three Y-stagger levels (0.50, 1.00, and 1.50 mm), and four Z-height mismatch levels (0.50, 1.00, 1.50, and 2.00 mm) were fabricated. Small deviations between the designed and realized dimensions were caused by printing tolerance and assembly clearance; therefore, the realized dimensions were recorded as ground-truth values for later comparison.

The two end-face topography defects were produced by precision milling along the Y axis of the copper coupons, both with a designed inclination angle of −15°. For the sawtooth (V-groove) defect, V-shaped ridges were machined on both copper end faces. For the single-sided inclined end-face defect, one coupon was machined into an inclined end face while the other coupon remained flat.

In total, three nominal pairs and 13 defect pairs covering the above categories were prepared, yielding 16 sample pairs for the experimental campaign.

3.3. Circular Test Fixture and Layout

To remake the circular arrangement of hairpin ends in a practical stator, the 16 sample pairs were mounted in a 300 mm diameter PLA circular fixture. The coupon pairs were evenly distributed around the circumference, with their end faces facing outward and their seams oriented radially. Figure 8 shows the fixture photograph and slot-numbering scheme, and Tables 1 and 2 list the defect assignment for all slots.

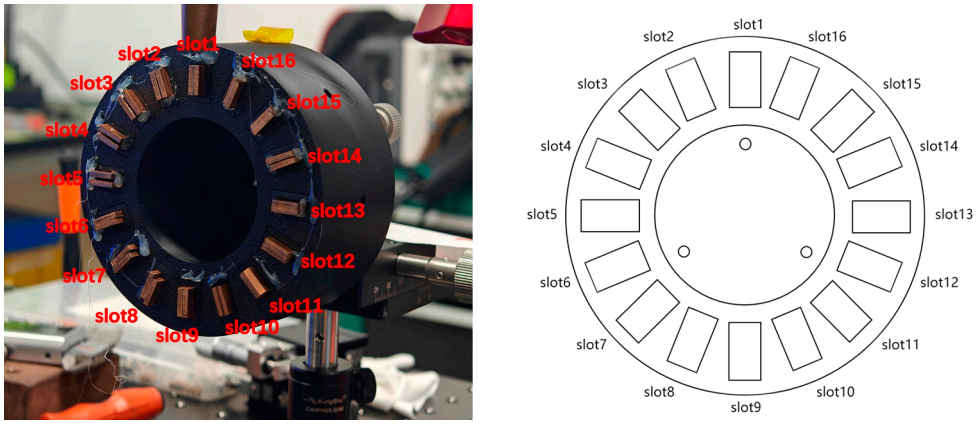


Figure 8. Circular test fixture and slot layout, showing the 3D-printed holder with 16 copper-coupon pairs mounted in an equally spaced configuration and the slot-numbering scheme.

Table 1. Defect sample assignment for slots 1–8 on the 3D-printed circular holder.

Slot No.	Slot 1	Slot 2	Slot 3	Slot 4	Slot 5	Slot 6	Slot 7	Slot 8
Defect Type	No defect	X-gap	X-gap	X-gap	X-gap	Y-stagger	Y-stagger	Y-stagger
Designed Parameter	/	0.25 mm	0.50 mm	0.75 mm	1.00 mm	0.50 mm	1.00 mm	1.50 mm
Actual Parameter	/	0.41 mm	0.75 mm	0.97 mm	1.16 mm	0.66 mm	1.07 mm	1.51 mm

Table 2. Defect sample assignment for slots 9–16 on the 3D-printed circular holder.

Slot No.	Slot 9	Slot 10	Slot 11	Slot 12	Slot 13	Slot 14	Slot 15	Slot 16
Defect Type	No defect	Sawtooth (V-groove) defect	Single-sided inclined end-face defect	No defect	Z-height mismatch	Z-height mismatch	Z-height mismatch	Z-height mismatch
Designed Parameter	/	−15°	−15°	/	0.50 mm	1.00 mm	1.50 mm	2.00 mm
Actual Parameter	/	−11°	−10°	/	0.53 mm	1.29 mm	1.53 mm	1.82 mm

3.4. Inspection Procedure

For each slot, the ring-light-illuminated visual channel and the OCT B-scan channel were triggered simultaneously by the central controller. The visual module identified the seam location and computed the Y-stagger, while the OCT channel performed a single B-scan of 2000 A-scans across the seam. The X-gap, Z-height mismatch, surface height range, and focus offset were then extracted using the method described in Section 2.3.

The OCT scanning position was fixed according to the predefined workpiece coordinate, reproducing the intended welding-station scenario. The nominal focal plane was defined as the zero-reference position of the OCT depth axis, and the focus offset, denoted as d_f, was defined as the axial displacement of the measured hairpin end-face position relative to this nominal focal plane. A positive d_f indicates that the measured end face is farther from the OCT probe than the nominal focal plane, whereas a negative d_f indicates that it is closer to the OCT probe. For the investigated hairpin-welding scenario, the process acceptance criteria were defined based on the allowable pre-weld alignment and focus tolerances established through cumulative process engineering experience with the laser welding setup and hairpin geometry used in this study, reflecting the geometric deviation magnitudes empirically regarded as acceptable for reliable weld formation under the applied welding parameters. Specifically, the pass/fail thresholds were $\Delta Z \leq 0.30$ mm, X-gap ≤ 0.30 mm, Y-stagger ≤ 0.50 mm, surface height range ≤ 0.50 mm, and $|d_f| \leq 0.30$ mm. A sample that violated any threshold was classified as defective. The OCT B-scan acquisition and depth-profile extraction were completed within the visual inspection time window, allowing the OCT channel to operate in parallel with the existing visual inspection step without extending the original production takt time.

4. Results

4.1. Joint Visual–OCT Inspection and Defect Detection Results

Figure 9 shows typical visual and OCT inspection results for the nominal pair and the five defect types.

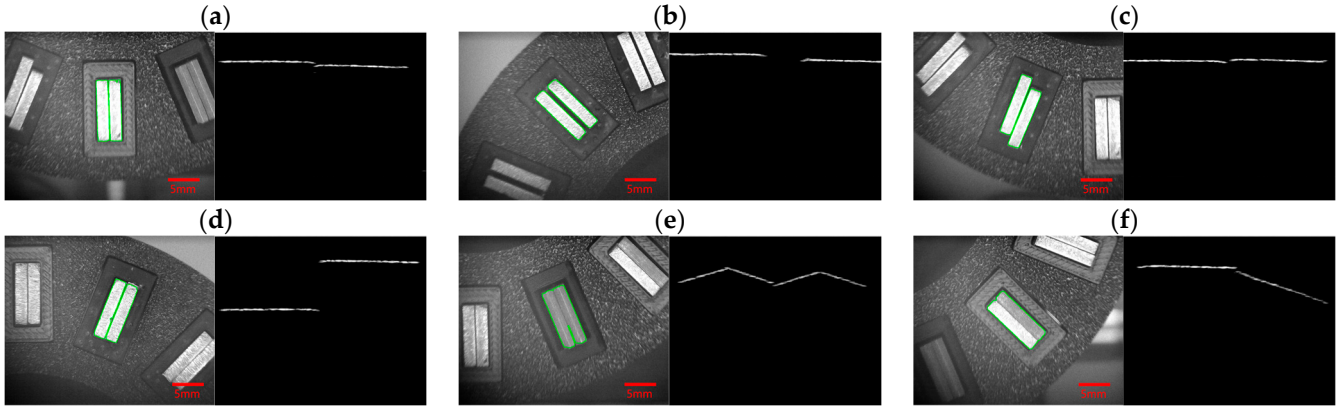


Figure 9. Visual and OCT inspection results for the defect-free nominal pair and the five defect types. In each subfigure, the left panel shows the coaxial camera image with extracted hairpin end-face contours, and the right panel presents the corresponding OCT B-scan. (**a**) Defect-free nominal pair. (**b**) X-gap defect. (**c**) Y-stagger defect. (**d**) Z-height mismatch defect. (**e**) Sawtooth (V-groove) defect. (**f**) Single-sided inclined end-face defect.

All 16 sample pairs mounted on the annular fixture were inspected using the parallel visual–OCT workflow. The measured values were compared with the preset pass/fail thresholds: X-gap ≤ 0.30 mm, Y-stagger ≤ 0.50 mm, Z-height mismatch ≤ 0.30 mm, surface height range ≤ 0.50 mm, and focus offset $|d_f| \leq 0.30$ mm. A sample was classified as defective

if any parameter exceeded its respective threshold. Table 3 summarizes the measurement results for slots 1–16. The "Actual Parameter" column lists the realized defect dimensions measured manually with a vernier caliper (resolution: 0.01 mm) after assembly.

Table 3. Defect detection results for slots 1–16.

Slot No.	Designed Defect Type	Actual Parameter (mm)	Measured X-Gap (mm)	Measured Y-Stagger (mm)	Measured Z-Mismatch (mm)	Measured Surface Height Range (mm)	Focus Offset from Nominal Focus (mm)	Detected Defect Type
Slot 1	No defect	/	0 *	0.155	0 *	0.131	−0.025	No defect
Slot 2	X-gap	0.41	0.421	0.108	0.037	0.066	−0.156	X-gap
Slot 3	X-gap	0.75	0.726	0.227	0.178	0.084	−0.049	X-gap
Slot 4	X-gap	0.97	1.036	0.176	0.084	0.066	+0.002	X-gap
Slot 5	X-gap	1.16	1.196	0.179	0.009	0.094	+0.150	X-gap
Slot 6	Y-stagger	0.66	0.071	0.696	0.019	0.056	−0.006	Y-stagger
Slot 7	Y-stagger	1.07	0 *	1.030	0 *	0.056	+0.123	Y-stagger
Slot 8	Y-stagger	1.51	0.062	1.501	0.066	0.075	+0.069	Y-stagger
Slot 9	No defect	/	0 *	0.083	0 *	0.125	+0.181	No defect
Slot 10	Sawtooth (V-groove)	/	0.004	0.236	0.075	0.525	+0.509	Surface defect + Defocus
Slot 11	Single-sided inclined end-face defect	/	0 *	0.315	0 *	1.134	+0.402	Surface defect + Defocus
Slot 12	No defect	/	0 *	0.163	0 *	0.228	+0.150	No defect
Slot 13	Z-height mismatch	0.53	0.009	0.297	0.497	0.066	+0.318	Z-mismatch + Defocus
Slot 14	Z-height mismatch	1.29	0.013	0.047	1.022	0.056	+0.335	Z-mismatch + Defocus
Slot 15	Z-height mismatch	1.53	0.004	0.018	1.537	0.047	+0.839	Z-mismatch + Defocus
Slot 16	Z-height mismatch	1.82	0.031	0.234	1.847	0.066	+0.789	Z-mismatch + Defocus

* No detectable gap or height mismatch was identified by the inspection algorithm within the measurement resolution, rather than an absolute physical value of zero.

The system correctly identified all 13 defective samples and classified the three nominal samples as defect-free, giving 100% classification accuracy for the predefined test set. The measured X-gap, Y-stagger, and Z-height mismatch values were close to the manually measured nominal parameters, with deviations mainly caused by differences between the manual measurement locations and the OCT/visual inspection positions. The sawtooth and single-sided inclined end-face defects were distinguished by the OCT-derived surface height range. The focus-offset criterion additionally flagged slots 10, 11, and 13–16 as defocused because their measured focus offsets exceeded the ±0.30 mm acceptable range.

To further quantify the agreement observed in Table 3, the relative error rate between the OCT-derived measurements and the manually measured actual parameters was calculated for each applicable slot. Given the limited number of samples per defect category, the resulting mean ± standard deviation should be interpreted as descriptive rather than statistically robust. The relative error rate was 3.9% ± 1.9% for X-gap ($n = 4$), 3.3% ± 2.5% for Y-stagger ($n = 3$), and 7.2% ± 9.4% for Z-height mismatch ($n = 4$). The comparatively large standard deviation for the Z-height mismatch category is driven primarily by Slot 14, for which the manual reference measurement and the fixed-position OCT B-scan are considered particularly susceptible to the positional-mismatch effect discussed below.

4.2. Error Analysis

Although all defects were correctly identified, errors between the OCT-derived values and the manually measured nominal values existed. The OCT channel provided an axial measurement accuracy with residual errors within ±15 μm during the calibration experiment, whereas the "actual" dimensions in the defect table were measured manually with a vernier caliper after assembly. These nominal values therefore include contact-position uncertainty, operator reading uncertainty, and local surface-selection uncertainty.

The dominant source of apparent error in the OCT axial metrics is the mismatch between the manual nominal location and the OCT sampling location. The caliper measurement was performed at a single accessible position on each sample, whereas the OCT value was extracted from the fixed B-scan cross-section used by the welding station. If the gap or height mismatch varies along the seam because of coupon tilt, fixture clearance, or milled-surface irregularity, the two measurements do not necessarily correspond to the same physical point.

A second contribution is the limited reliability of the manually measured ground truth. Although the caliper resolution is 0.01 mm, the effective uncertainty is larger for narrow gaps, stepped copper end faces, and sloped or rough surfaces because the caliper jaws may not contact the same feature used by the OCT peak-detection algorithm. Consequently, part of the apparent OCT error reflects nominal-measurement uncertainty rather than intrinsic OCT depth-measurement noise.

Fixture-related deviations also contribute to the comparison error. The 3D-printed holders introduce geometric tolerances, and residual clearance can allow a coupon to tilt slightly before fastening. Such tilt changes the local gap and height along the seam, so a single OCT B-scan may reasonably differ from a caliper reading taken elsewhere on the sample.

The visual Y-stagger error is secondary in this study and is mainly governed by image-edge contrast, thresholding stability, and pixel resolution. Overall, the observed deviations are acceptable for the intended pass/fail thresholds, which are much larger than the calibrated OCT axial repeatability. Future validation should use a co-located nominal method, such as calibrated step artifacts or microscope/profilometer measurements at the same B-scan position, to separate OCT measurement error from manual-nominal uncertainty.

4.3. Quantitative Uncertainty Analysis of OCT and Reference Measurements

To quantify the discrepancies discussed qualitatively in Section 4.2, a two-part quantitative uncertainty analysis was performed for the three geometric parameters directly comparable to caliper-based reference values; namely, X-gap, Y-stagger, and Z-height mismatch (slots 2–8 and 13–16 in Table 3). The two end-face topography defects were excluded from this quantitative comparison, as their non-planar geometry precludes a well-defined caliper reference measurement.

An agreement analysis between the OCT-derived and caliper reference measurements was performed for each of the three parameter categories, in which the difference between the OCT-derived value and the corresponding caliper reference value was computed for every applicable slot:

$$d_i = X_{OCT,i} - X_{ref,i} \quad (1)$$

where $X_{OCT,i}$ and $X_{ref,i}$ denote the OCT-derived and caliper-measured values, respectively, for slot i. For each parameter category, the mean difference (bias, $\bar{d}$) and the standard deviation of the differences (SD_d) were calculated, and the 95% limits of agreement (LoA) were obtained as:

$$LoA = \bar{d} \pm 1.96 \times SD_d \quad (2)$$

For the X-gap category, the mean bias was $\bar{d}_X = 0.022$ mm with $SD_d = 0.038$ mm, corresponding to 95% limits of agreement of −0.052 to 0.096 mm. For the Y-stagger category, $\bar{d}_Y = -0.004$ mm ($SD_d = 0.038$ mm), and for the Z-height mismatch category, $\bar{d}_Z = -0.067$ mm ($SD_d = 0.136$ mm). In all three categories, the magnitude of the mean bias was small relative to the corresponding process acceptance threshold (0.30 mm), indicating that the two measurement approaches are, on average, in good agreement; the width of the 95% limits of agreement, however, exceeds the ±15 µm axial repeatability established for the OCT channel in Section 2.2 by more than an order of magnitude, consistent with the hypothesis that the reference (caliper) measurement, rather than the OCT channel, dominates the observed dispersion.

To further isolate the contribution of each measurement method to the observed discrepancy, a standard uncertainty budget was constructed for both the OCT channel and the caliper-based reference measurement, following the Type A/Type B classification of the Guide to the Expression of Uncertainty in Measurement (GUM).

The combined standard uncertainty of the OCT channel, $u_c(OCT)$, was obtained from two components already characterized in Section 2.2: (i) a Type A component, $u_A(OCT)$, taken as the standard deviation of the 2000 consecutive A-scan measurements at each stepped position (Figure 4c); and (ii) a Type B component, $u_B(OCT)$, taken as the RMS residual of the axial linearity measurement over the 4.5 mm working range (Figure 4b, corresponding to the reported ±15 µm figure). The two components were combined in quadrature:

$$u_c(OCT) = \sqrt{u_A(OCT)^2 + u_B(OCT)^2} \quad (3)$$

yielding $u_c(OCT) = 13.412$ µm, and an expanded uncertainty $U(OCT) = k * u_c(OCT) = 26.824$ µm at a coverage factor of $k = 2$ (approximately 95% confidence).

The combined standard uncertainty of the caliper-based reference measurement, $u_c(ref)$, was evaluated from two components. The first is a Type B component associated with the instrument resolution (0.01 mm), modeled as a rectangular distribution:

$$u_{resolution} = \frac{0.01 \text{ mm}}{2\sqrt{3}} = 2.887 \text{ µm} \quad (4)$$

The second is a Type A component, $u_A(ref)$, obtained from repeated caliper measurements. For each of the applicable slots, the X-gap, Y-stagger, or Z-height mismatch was independently re-measured 10 times by the same operator, and the pooled standard deviation across all repeated measurements was taken as $u_A(ref) = 32.384$ µm. The two components were combined in quadrature:

$$u_c(ref) = \sqrt{u_{resolution}^2 + u_A(ref)^2} \quad (5)$$

yielding $u_c(ref) = 32.512$ µm.

Since the OCT and reference measurements are independent, the uncertainty of their difference is given by:

$$u_{combined} = \sqrt{u_c(OCT)^2 + u_c(ref)^2},\ U_{combined} = k \cdot u_{combined} \quad (6)$$

which gives $u_{combined}$ = 70.339 µm at k = 2. Comparing this value with the per-slot residuals reported in Table 3, most residuals remained well within the combined expanded uncertainty of 70.339 µm, indicating that they are statistically consistent with the combined measurement uncertainty of the two methods. One slot, however, exhibited a residual of approximately 268 µm, substantially exceeding $u_{combined}$ by nearly a factor of four; this outlier cannot be explained by the measurement uncertainty of either method alone and is instead attributed to the positional mismatch between the fixed OCT B-scan location and the manually selected caliper contact point discussed in Section 4.2, likely compounded by local sample-specific factors (e.g., coupon tilt or surface irregularity) at that particular slot.

Taken together, the dispersion observed between the OCT-derived and manually measured geometric parameters is dominated by the uncertainty of the caliper-based reference measurement rather than by the intrinsic measurement uncertainty of the OCT channel, consistent with the qualitative discussion in Section 4.2.

5. Discussion

The characterization results in Section 2.2 indicate that the coaxial OCT–vision system provides adequate metrological margin for the process tolerances defined in Section 3.4. The OCT channel achieved axial residual errors within ±15 µm and short-term repeatability better than ±10 µm, while the visual channel achieved a lateral accuracy within ±30 µm; both figures are approximately an order of magnitude smaller than the corresponding pass/fail thresholds (0.30–0.50 mm). This margin suggests that classification reliability in the present study is governed primarily by the tolerance design rather than by sensor-level noise, and that the system would likely retain sufficient headroom under moderately tighter industrial specifications. Nonetheless, the 100% classification accuracy obtained on the 16 mock-up pairs should be regarded as a demonstration of feasibility rather than a statistically validated production-scale detection rate, given the limited sample size and the use of 3D-printed rather than production-representative fixtures.

The discrepancies between the OCT-derived parameters and the manually measured "actual" values in Table 3 merit further comment, as they substantially exceed the ±15 µm axial repeatability established for the OCT channel and therefore cannot be attributed to the OCT measurement itself. Several factors likely contribute. The caliper measurement was taken at a single accessible location on each sample, whereas the OCT value was extracted from a fixed B-scan cross-section aligned with the welding coordinate; where gap or height varies along the seam due to coupon tilt or local surface irregularity, the two methods need not sample the same physical point. In addition, caliper measurement uncertainty is inherently larger for narrow gaps and sloped or stepped end faces, where the jaws may not consistently contact the surface feature identified by the OCT peak-detection algorithm, and residual clearance in the 3D-printed fixtures can permit slight coupon tilt prior to fastening. Taken together, these factors indicate that the observed discrepancies primarily reflect uncertainty in the manual ground-truth procedure rather than a limitation of the proposed inspection method. A more rigorous validation would employ a co-located, metrology-grade reference artifact measured at the identical B-scan position to decouple these two sources of error.

The present study also has several limitations. The OCT channel acquires a single, fixed-position B-scan rather than a full end-face C-scan, so localized defects outside the scanned line may not be captured. The relationship between the ~900 mm working distance

and measurement precision was not isolated in the present characterization and merits dedicated investigation, as working distance can interact with spot size, depth of focus, and mechanical stability. Finally, the system was evaluated under controlled laboratory conditions on fixture-mounted mock-ups rather than on an active welding line, where vibration, thermal drift, and surface contamination may affect performance.

Future work will therefore focus on validating the method on production-representative hairpin stators with a larger and more diverse sample set, including cases near the pass/fail thresholds; extending the acquisition strategy toward multi-line or C-scan profiling to improve end-face coverage without exceeding the production takt time; employing calibrated reference artifacts to separate intrinsic OCT uncertainty from ground-truth error; and conducting on-line trials to assess robustness under realistic manufacturing conditions.

6. Conclusions

This study developed a coaxial OCT–visual inspection system for pre-weld alignment assessment of hairpin ends in EV stator manufacturing. By integrating SD-OCT, visual, and laser welding channels along a common optical axis, the system enables parallel multimodal inspection without extending production takt time. At a ~900 mm focus distance, the OCT subsystem achieved axial residual errors within ±15 μm over a 4.5 mm working range, and a single-A-scan peak-to-background contrast of 21.7 dB. Experiments on 16 hairpin mock-ups demonstrated that the OCT channel effectively detects X-gap, Z-height mismatch, topography defects, and focus offset, while the visual branch provides Y-stagger evaluation, successfully classifying all nominal and defective samples. This non-contact approach offers a high-precision, rapid geometric qualification solution for hairpin laser welding.

Author Contributions: Conceptualization, Y.D.; Methodology, Y.W., B.W., L.X. and Y.D.; Software, Y.W., L.X. and Y.D.; Validation, Y.W., X.L. and Y.D.; Formal analysis, Y.W., B.W., L.X. and Y.D.; Investigation, Y.D.; Resources, Q.C., X.H., J.W. and Y.D.; Data curation, Y.W., B.W. and Y.D.; Writing—original draft, Y.W.; Writing—review & editing, X.L. and Y.D.; Project administration, Y.D.; Funding acquisition, Q.C., X.H., J.W. and Y.D. All authors have read and agreed to the published version of the manuscript.

Funding: The financial support of the National Natural Science Foundation of China under Grant 62303093 and Wenzhou Major Scientific and Technological Innovation Research Project ZG2024036 is acknowledged.

Institutional Review Board Statement: Not applicable.

Informed Consent Statement: Not applicable.

Data Availability Statement: The raw data supporting the conclusions of this article will be made available by the authors on request.

Acknowledgments: During the preparation of this work, the authors used Claude Sonnet 5.5 (Anthropic) in order to improve language, check grammar, and refine wording. After using this tool, the authors reviewed and edited the content as needed and take full responsibility for the content of the publication.

Conflicts of Interest: The authors declare no conflicts of interest.

References

1. Rajendran, G.; Raute, R.; Caruana, C.; Andriukaitis, D. Bridging Innovation and Sustainability: The Strategic Role of High-Efficiency Motors in Advancing Industry 5.0. *Energies* **2026**, *19*, 1003. [CrossRef]
2. Li, Y.; Ouyang, M.; Chan, C.C.; Sun, X.; Song, Y.; Cai, W. Key Technologies and Prospects for Electric Vehicles Within Emerging Power Systems: Insights from Five Aspects. *CSEE J. Power Energy Syst.* **2024**, *10*, 439–447. [CrossRef]

3. Zou, T.; Gerada, D.; La Rocca, A.; Moslemin, M.; Cairns, A.; Cui, M. A Comprehensive Design Guideline of Hairpin Windings for High Power Density Electric Vehicle Traction Motors. *IEEE Trans. Transp. Electrif.* **2022**, *8*, 3578–3593. [CrossRef]
4. Arzillo, A.; Braglia, P.; Nuzzo, S.; Barater, D.; Franceschini, G.; Gerada, D. Challenges and Future Opportunities of Hairpin Technologies. In Proceedings of the 2020 IEEE 29th International Symposium on Industrial Electronics (ISIE), Delft, The Netherlands, 17–19 June 2020; pp. 277–282.
5. Glaessel, T.; Seefried, J.; Franke, J. Challenges in the manufacturing of hairpin windings and application opportunities of infrared lasers for the contacting process. In Proceedings of the 2017 7th International Electric Drives Production Conference (EDPC), Würzburg, Germany, 5–6 December 2017; pp. 1–7.
6. Kampker, A.; Dorn, B.; Brans, F.; Stäck, C.; Windhausen, M.; Patil, K.V. Analysis of the Behaviour of the Winding Head of a Hairpin Stator. In Proceedings of the 2022 12th International Electric Drives Production Conference (EDPC), Regensburg, Germany, 29–30 November 2022; pp. 1–9.
7. Zhu, T.; Zhang, C.; Yin, Y. A novel interpolator designed for laser scanning welding of hairpin windings in electric vehicle motors. *Int. J. Adv. Manuf. Technol.* **2024**, *133*, 3225–3237. [CrossRef]
8. Kampker, A.; Heimes, H.H.; Dorn, B.; Brans, F.; Hartmann, S.; Schaffrath, M. Effects of the Reduction of the Copper Wire Cross-Section on the Welding Process in the Manufacturing of Hairpin Stators for Electric Traction Motors. In Proceedings of the 2022 12th International Electric Drives Production Conference (EDPC), Regensburg, Germany, 29–30 November 2022; pp. 1–9.
9. Botros, R.A.; Pari, M.T.; Fortunato, A.; Ceglarek, D.; Paolini, B.; Franciosa, P. Effect of Static Laser Beam Shaping on Lateral and Vertical Gap Bridging for Welding of Rectangular Copper Hairpin Windings. In Proceedings of the ASME 2024 19th International Manufacturing Science and Engineering Conference, Knoxville, TN, USA, 17–21 June 2024.
10. Maleki, P.; Akhavan-Safar, A.; Carbas, R.J.; Marques, E.A.; da Silva, L.F. A comprehensive review of failures in bi-material interfaces: Mechanisms, prediction, and mitigation strategies. *Proc. Inst. Mech. Eng. Part L J. Mater. Des. Appl.* **2026**, *OnlineFirst*. [CrossRef]
11. Portos, J.; Dean, K.; Parker, B.; Cannon, J. Most common mechanisms and reasons for electric motor failures in industry. In Proceedings of the 2019 IEEE IAS Pulp, Paper and Forest Industries Conference (PPFIC), Jacksonville, FL, USA, 23–28 June 2019; pp. 1–11.
12. Yu, H.; Yin, Y.; Ji, S.; Zhang, C.; Zhu, T.; Liu, Z. Laser welding method and quality analysis of hairpin windings based on visual recognition of gap and displacement matching process. *Opt. Laser Technol.* **2024**, *178*, 111224. [CrossRef]
13. Stavropoulos, P.; Sabatakakis, K.; Bikas, H. Welding challenges and quality assurance in electric vehicle battery pack manufacturing. *Batteries* **2024**, *10*, 146. [CrossRef]
14. Regaard, B.; Kaierle, S.; Poprawe, R. Seam-tracking for high precision laser welding applications—Methods, restrictions and enhanced concepts. *J. Laser Appl.* **2009**, *21*, 183–195. [CrossRef]
15. Wang, H.; Fang, R.; Jiang, H.; Liu, Y.; Zhao, X.; Chen, C. Structured light vision-based online quality inspection of weld formation for arc-welded joints in steel. *Opt. Lasers Eng.* **2025**, *191*, 108991. [CrossRef]
16. Li, B.; Xu, Z.; Gao, F.; Cao, Y.; Dong, Q. 3D Reconstruction of High Reflective Welding Surface Based on Binocular Structured Light Stereo Vision. *Machines* **2022**, *10*, 159. [CrossRef]
17. Amir, Y.M.; Thörnberg, B. High Precision Laser Scanning of Metallic Surfaces. *Int. J. Opt.* **2017**, *2017*, 4134205. [CrossRef]
18. Kahatapitiya, N.S.; Saleah, S.A.; Seong, D.; Ravichandran, N.K.; Han, S.; Wijesinghe, R.E.; Kim, J. Optical Coherence Tomography for High-Precision Industrial Inspection in Industry 4.0: Advances, Challenges, and Future Trends. *Laser Photonics Rev.* **2026**, *20*, e02290. [CrossRef]
19. Guan, G.; Hirsch, M.; Syam, W.P.; Leach, R.K.; Huang, Z.; Clare, A.T. Loose powder detection and surface characterization in selective laser sintering via optical coherence tomography. *Proc. R. Soc. A Math. Phys. Eng. Sci.* **2016**, *472*, 20160201. [CrossRef] [PubMed]
20. Antoniuk, P.; Strąkowski, M.; Pluciński, J.; Kosmowski, B. Non-Destructive Inspection of Anti-corrosion protective coatings using optical coherent tomography. *Metrol. Meas. Syst.* **2012**, *XIX*, 365–372. [CrossRef]
21. Joo, K.-N.; Park, H.-M. Recent Progress on Optical Tomographic Technology for Measurements and Inspections of Film Structures. *Micromachines* **2022**, *13*, 1074. [CrossRef] [PubMed]
22. Agrawal, A.; Chen, C.-W.; Baxi, J.; Chen, Y.; Pfefer, T.J. Multilayer thin-film phantoms for axial contrast transfer function measurement in optical coherence tomography. *Biomed. Opt. Express* **2013**, *4*, 1166–1175. [CrossRef] [PubMed]
23. Kwon, I.H.; Kim, H.S.; Kim, D.Y.; Lee, H.J.; Lee, S.W. Utilizing optical phantoms for biomedical-optics technology: Recent advances and challenges. *Curr. Opt. Photonics* **2024**, *8*, 327–344.
24. Lal, C. Advancements in Structural and Functional Imaging Using Fourier Domain Optical Coherence Tomography. Doctoral Dissertation, NUI Galway, Galway, Ireland, 2020.
25. Popescu, D.P.; Choo-Smith, L.P.I.; Flueraru, C.; Mao, Y.; Chang, S.; Disano, J.; Sowa, M.G. Optical coherence tomography: Fundamental principles, instrumental designs and biomedical applications. *Biophys. Rev.* **2011**, *3*, 155–169. [CrossRef] [PubMed]
26. Lee, B.S.; Strand, T.C. Profilometry with a coherence scanning microscope. *Appl. Opt.* **1990**, *29*, 3784–3788. [CrossRef] [PubMed]

27. de Groot, P. Coherence Scanning Interferometry. In *Optical Measurement of Surface Topography*; Leach, R., Ed.; Springer: Berlin/Heidelberg, Germany, 2011; pp. 187–208.
28. Wang, Z.; Potsaid, B.; Chen, L.; Doerr, C.; Lee, H.-C.; Nielson, T.; Jayaraman, V.; Cable, A.E.; Swanson, E.; Fujimoto, J.G. Cubic meter volume optical coherence tomography. *Optica* **2016**, *3*, 1496–1503. [CrossRef] [PubMed]
29. Dupriez, N.D.; Truckenbrodt, C. OCT for Efficient High Quality Laser Welding. *Laser Tech. J.* **2016**, *13*, 37–41. [CrossRef]
30. Will, T.; Jeron, T.; Hoelbling, C.; Müller, L.; Schmidt, M. In-Process Analysis of Melt Pool Fluctuations with Scanning Optical Coherence Tomography for Laser Welding of Copper for Quality Monitoring. *Micromachines* **2022**, *13*, 1937. [CrossRef] [PubMed]
31. Sokolov, M.; Franciosa, P.; Sun, T.; Ceglarek, D.; Dimatteo, V.; Ascari, A.; Fortunato, A.; Nagel, F. Applying optical coherence tomography for weld depth monitoring in remote laser welding of automotive battery tab connectors. *J. Laser Appl.* **2021**, *33*, 012028. [CrossRef]
32. Mattulat, T. Understanding the coaxial optical coherence tomography signal during the laser welding of hidden T-joints. *J. Laser Appl.* **2024**, *36*, 012003. [CrossRef]
33. Kim, H.; Kim, C.; Kang, M. Interfacial Gap Prediction in Laser Welding of Pure Copper Overlap Joints Using Multiple Sensors. *Materials* **2025**, *18*, 5189. [CrossRef] [PubMed]
34. Wu, D.; Zhang, P.; Shi, H.; Lu, Q.; Yu, Z.; Huang, Y. Advancements and prospects of OCT-enabled all-process monitoring and inline quality assurance in laser keyhole welding: A critical review. *J. Manuf. Process.* **2025**, *152*, 1179–1203. [CrossRef]
35. Baader, M.; Mayr, A.; Raffin, T.; Selzam, J.; Kühl, A.; Franke, J. Potentials of Optical Coherence Tomography for Process Monitoring in Laser Welding of Hairpin Windings. In Proceedings of the 2021 11th International Electric Drives Production Conference (EDPC), Erlangen, Germany, 7–9 December 2021; pp. 1–10.
36. Rapp, J.; Mansour, H.; Boufounos, P.; Koike-Akino, T.; Parsons, K. Multi-layered surface estimation for low-cost optical coherence tomography. *IEEE Trans. Comput. Imaging* **2024**, *10*, 1706–1721. [CrossRef]

Disclaimer/Publisher's Note: The statements, opinions and data contained in all publications are solely those of the individual author(s) and contributor(s) and not of MDPI and/or the editor(s). MDPI and/or the editor(s) disclaim responsibility for any injury to people or property resulting from any ideas, methods, instructions or products referred to in the content.